

## NEUROTECHNOLOGY

## Development of a neural interface for high-definition, long-term recording in rodents and nonhuman primates

Chia-Han Chiang<sup>1\*†</sup>, Sang Min Won<sup>2\*</sup>, Amy L. Orsborn<sup>3,4,5\*</sup>, Ki Jun Yu<sup>6\*</sup>, Michael Trumpis<sup>1</sup>, Brinnae Bent<sup>1</sup>, Charles Wang<sup>1</sup>, Yeguang Xue<sup>7,8</sup>, Seunghwan Min<sup>9</sup>, Virginia Woods<sup>1</sup>, Chunxiu Yu<sup>1,10</sup>, Bong Hoon Kim<sup>11,12</sup>, Sung Bong Kim<sup>13</sup>, Rizwan Huq<sup>14</sup>, Jinghua Li<sup>13,15,16</sup>, Kyung Jin Seo<sup>17</sup>, Flavia Vitale<sup>18,19</sup>, Andrew Richardson<sup>20</sup>, Hui Fang<sup>17</sup>, Yonggang Huang<sup>7,8,13,21</sup>, Kenneth Shepard<sup>14,22</sup>, Bijan Pesaran<sup>3,23†</sup>, John A. Rogers<sup>7,8,13,15,21,24,25,26,27†</sup>, Jonathan Viventi<sup>1,28,29†</sup>

Long-lasting, high-resolution neural interfaces that are ultrathin and flexible are essential for precise brain mapping and high-performance neuroprosthetic systems. Scaling to sample thousands of sites across large brain regions requires integrating powered electronics to multiplex many electrodes to a few external wires. However, existing multiplexed electrode arrays rely on encapsulation strategies that have limited implant lifetimes. Here, we developed a flexible, multiplexed electrode array, called “Neural Matrix,” that provides stable in vivo neural recordings in rodents and nonhuman primates. Neural Matrix lasts over a year and samples a centimeter-scale brain region using over a thousand channels. The long-lasting encapsulation (projected to last at least 6 years), scalable device design, and iterative in vivo optimization described here are essential components to overcoming current hurdles facing next-generation neural technologies.

## INTRODUCTION

Current neural interface devices sample the brain coarsely or are restricted to sampling a small neuronal volume because they have a limited number of sensing contacts (typically ~100) (table S1). Increasing interface throughput to densely and simultaneously sample

large areas of the brain with high fidelity is a pressing need for research and clinical neural interfaces (1). Achieving this increase in density and coverage requires substantially more sensing contacts. Sampling thousands (kilo-scale) to millions (mega-scale) of contacts simultaneously over a centimeter-scale area can meet this demand.

Scaling microfabricated neural interfaces presents a technical challenge: Individually wiring thousands or millions of electrodes is infeasible. Kilo-scale and mega-scale devices require powered multiplexing electronics directly integrated into the sensor to eliminate wiring bottlenecks and enable scalable electrode arrays (2–4) with compact packaging. Until now, these active electrode arrays (with integrated, powered electronics) have suffered from limited implant lifetimes because of encapsulation failure; voltage differentials between powered metal lines in the device and the biological environment accelerate the failure of polymer-based encapsulation (5). Encapsulation failures—even single pin-hole defects—introduce current leakage from the device into the brain, which results in both device failure and tissue damage (6, 7). These failures have prevented long-term in vivo use.

Optimization of kilo-scale devices is subject to numerous failure modes, necessitating iterative testing. Testing large-area devices must be done in animal models relevant for human translation, such as in nonhuman primates (NHPs) performing behavioral tasks. However, traditional testing paradigms for chronic implantable devices typically involve testing only one or two device iterations per animal, which is impractical for high-throughput technology development.

Here, we present an actively multiplexed, matrix electrode array, called Neural Matrix, that addresses the challenges of scalability, longevity, and device optimization in vivo for kilo-scale neural interfaces. Although our approach can be generalized to other active bio-interfaces, including both penetrating and surface electrodes, we focused on surface micro-electrocorticography (μECoG) devices. Ultrathin (<30 μm) and flexible μECoG electrode arrays can maintain signal quality over long periods of time with little tissue injury or irritation after implantation (8, 9). μECoG arrays can also sample neural activity densely, revealing rich spatial and temporal information hidden by traditional approaches such as electroencephalography and conventional ECoG (4, 10).

<sup>1</sup>Department of Biomedical Engineering, Duke University, Durham, NC 27708, USA.

<sup>2</sup>Department of Electrical and Computer Engineering, Sungkyunkwan University, Suwon 16419, Republic of Korea. <sup>3</sup>Center for Neural Science, New York University, New York, NY 10003, USA. <sup>4</sup>Department of Electrical and Computer Engineering, University of Washington, Seattle, WA 98195, USA. <sup>5</sup>Department of Bioengineering, University of Washington, Seattle, WA 98195, USA. <sup>6</sup>School of Electrical and Electronic Engineering, Yonsei University, Seoul 03722, Republic of Korea. <sup>7</sup>Department of Civil and Environmental Engineering, Northwestern University, Evanston, IL 60208, USA. <sup>8</sup>Department of Mechanical Engineering, Northwestern University, Evanston, IL 60208, USA.

<sup>9</sup>Department of Electrical and Computer Engineering, University of Wisconsin–Madison, Madison, WI 53706, USA. <sup>10</sup>Department of Biological Science, Michigan Technological University, Houghton, MI 49931, USA. <sup>11</sup>Department of Organic Materials and Fiber Engineering, Soongsil University, Seoul 06978, Republic of Korea. <sup>12</sup>Department of Information Communication, Materials, and Chemistry Convergence Technology, Soongsil University, Seoul 06978, Republic of Korea. <sup>13</sup>Materials Science and Engineering, Northwestern University, Evanston, IL 60208, USA. <sup>14</sup>Department of Electrical Engineering, Columbia University, New York, NY 10027, USA. <sup>15</sup>Department of Materials Science and Engineering, University of Illinois at Urbana-Champaign, Urbana, IL 61801, USA. <sup>16</sup>Department of Materials Science and Engineering, Center for Chronic Brain Injury, The Ohio State University, Columbus, OH 43210, USA.

<sup>17</sup>Department of Electrical and Computer Engineering, Northeastern University, Boston, MA 02115, USA. <sup>18</sup>Department of Neurology, Department of Bioengineering, Department of Physical Medicine & Rehabilitation, Center for Neuroengineering and Therapeutics, University of Pennsylvania, PA 19104, USA. <sup>19</sup>Center of Neurotrauma, Neurodegeneration, and Restoration, Corporal Michael J. Crescenzo Veterans Affairs Medical Center, Philadelphia, PA 19104, USA. <sup>20</sup>Department of Neurosurgery, University of Pennsylvania, Philadelphia, PA 19104, USA. <sup>21</sup>Center for Bio-integrated Electronics, Northwestern University, Evanston, IL 60208, USA. <sup>22</sup>Department of Biomedical Engineering, Columbia University, New York, NY 10027, USA. <sup>23</sup>Department of Neurology, NYU Langone Health, New York, NY 10016, USA. <sup>24</sup>Simpson Querrey Institute, Northwestern University, Chicago, IL 60611, USA. <sup>25</sup>Department of Biomedical Engineering, Northwestern University, Evanston, IL 60208, USA. <sup>26</sup>Department of Chemistry, Northwestern University, Evanston, IL 60208, USA. <sup>27</sup>Department of Neurological Surgery, Feinberg School of Medicine, Northwestern University, Chicago, IL 60611, USA. <sup>28</sup>Department of Neurobiology, Duke University, Durham, NC 27708, USA. <sup>29</sup>Department of Neurosurgery, Duke University, Durham, NC 27708, USA.

\*These authors contributed equally to this work.  
†Corresponding author. Email: j.viventi@duke.edu (J.V.); jrogers@northwestern.edu (J.A.R.); bijan@nyu.edu (B.P.); kenchiangch@gmail.com (C.-H.C.)

†Corresponding author. Email: j.viventi@duke.edu (J.V.); jrogers@northwestern.edu (J.A.R.); bijan@nyu.edu (B.P.); kenchiangch@gmail.com (C.-H.C.)

†Corresponding author. Email: j.viventi@duke.edu (J.V.); jrogers@northwestern.edu (J.A.R.); bijan@nyu.edu (B.P.); kenchiangch@gmail.com (C.-H.C.)

†Corresponding author. Email: j.viventi@duke.edu (J.V.); jrogers@northwestern.edu (J.A.R.); bijan@nyu.edu (B.P.); kenchiangch@gmail.com (C.-H.C.)

Our device reached high channel count while maintaining high electrode sampling density. We designed and fabricated Neural Matrix electrodes and tested them in rodents and NHPs. We developed a small,  $8 \times 8$  electrode array to evaluate the performance of capacitive sensing and the long-term stability in rodents, and a kiloscale,  $28 \times 36$  electrode Neural Matrix array to demonstrate scalability and neural signal recording in NHPs.

## RESULTS

### Electrode array design and fabrication

The fabrication of the active electrode arrays builds on our recent advances in flexible, capacitively coupled arrays, in which thermally grown silicon dioxide (t-SiO<sub>2</sub>) serves not only as the biofluid barrier (on the front and back sides), but also as the dielectric medium for capacitive coupling between the brain and electrode contacts (on the front side). T-SiO<sub>2</sub> encapsulation provides a robust, bendable, and ultrathin (~1 μm) moisture barrier that is free of pinhole defects and, unlike polymer-based encapsulation, is reliable while devices are powered with direct current (dc) bias voltages (5, 11). Capacitive sensing further improved the encapsulation (12) by eliminating feedthroughs that accelerate leak current formation and eliminated concerns over metal corrosion. Accelerated aging projected device life span up to 60 years (5, 13, 14).

In the kilo-scale Neural Matrix array, two layers of metal interconnects and embedded multiplexers enabled recording from 1008 electrodes (28 columns and 36 rows) at high density, while covering an area of  $9 \times 9.24 \text{ mm}^2$  (Fig. 1, A to C). Within each unit cell, a constant current sink external to the array and a transistor (fig. S1, A to D) with a capacitively coupled input (T1 in Fig. 1D) formed a source-follower amplifier whose output was buffered and recorded. The buffered output was also alternating current (ac) coupled to a new dc potential (AS in Fig. 1D) and was applied to the corresponding drain connection of the source-follower transistor. This enabled active shielding, reducing the effect of parasitic drain-gate capacitances and improving the overall gain of the circuit. Another transistor (T2 in Fig. 1D), within the unit cell, multiplexed all the electrodes in a column to share a common output wire. In this manner, the total number of wires needed was  $2C + R$ , where  $C$  is the number of columns and  $R$  is the number of rows in the array. The total number of wires could be further reduced by increasing the multiplexing ratio and/or integrating the active shielding circuitry into the flexible array with additional transistors. In vitro soak testing in a phosphate-buffered solution revealed high yield (99.8%) and uniform voltage gain (0.88, where 1 is ideal) throughout the kilo-scale array (Fig. 1E).

Flexibility and resistance to mechanical fatigue are critical for a robust implantable system. The Neural Matrix arrays were only 29 μm thick in the sensing area (fig. S1E), resulting in minimal induced strains on each layer during bending (Fig. 1F). Finite element analysis (FEA) indicated that the maximum strain induced in the Si, t-SiO<sub>2</sub>, and metal layers for a 2.5-mm bend radius was less than 0.2%, below the fracture limit (~1%) (Fig. 1G). Repeated mechanical cycling of the device up to 10,000 cycles to a minimum bend radius of 2.5 mm showed no change in yield or increase in leakage current (fig. S1F).

### Neural matrix array validation in rats

We fabricated a smaller ( $8 \times 8$ ) Neural Matrix array to evaluate the performance of capacitive sensing and the long-term stability of the t-SiO<sub>2</sub> encapsulation in rodents. The electrode array included

64 channels arranged in an  $8 \times 8$  grid with an electrode pitch of 400 μm. This size and density were chosen to match our previously published passive electrode arrays, which used traditional faradaic sensing (15, 16), to allow direct comparison of the acquired signals. In an acute experiment, we implanted the Neural Matrix electrode epidurally over the rat auditory cortex (Fig. 2A), sampling electrical activity from a  $\sim 3.2 \times 3.2 \text{ mm}^2$  area of the brain. Field potentials were recorded from an anesthetized rat during (i) pseudorandomized presentation of 50-ms tone pips ranging from 0.5 to 32 kHz, and (ii) 0.2-ms broadband click sound stimuli. A 3-s example of a single channel in the array, bandpass filtered to 2 to 100 Hz, shows clear responses evoked by click sounds (Fig. 2B).

To verify that electrodes in the Neural Matrix array provided spatially varying measurement of electrical activity in the brain, we calculated the spatial semivariogram. Spatial semivariogram analysis measured the dissimilarity of the signals as a function of distance and indicated a spatially varying random field with covariance properties that were well described by the Matérn covariance model. The length scale (2.49 mm), smoothness (0.73), and amplitude (~115 μVrms) of the variance model were consistent with rat auditory cortex potentials previously observed using passive arrays (fig. S2, A and B) (16), whereas the notable vertical shift in semivariance reflects the higher noise in the active device (~58 μVrms, 2 to 100 Hz) (Fig. 2C).

The spatial specificity suggested by the semivariogram was also evident in the spatially organized tone preference of sites. Examples of mean and single-trial responses for the best-tuned frequency at two sites on the array are shown in Fig. 2D. These two sites are located ~1.44 mm apart and respond most strongly to pure-tone stimuli of different frequencies (locations marked in Fig. 2E). The best-tuned frequency at each site was determined by mapping each tuning curve's center of mass at each electrode site. Tuning values were calculated using the Mahalanobis distance of tone responses from the mean and covariance of baseline vectors. The best frequency tonotopic map of the array recapitulated the expected tonotopy of the primary auditory cortex (Fig. 2E) (15–17).

We further characterized the sensitivity to auditory stimuli by measuring the evoked signal-to-noise ratio (ESNR), which is the ratio of Mahalanobis distances for evoked responses versus the distances computed for baseline vectors. The spatial distribution of highly versus moderately evoked sites matched the ESNR mapped in an earlier passive recording under similar preparation (Fig. 2F) (16). However, the median ESNR was 2.4 dB lower in the active recording, presumably because of higher baseline variance introduced by electronic noise caused by increased noise in the fabricated silicon transistors (fig. S2C).

Last, to evaluate the quality of the neural signals recorded from the Neural Matrix array, we used a principal components analysis and linear discriminant analysis (PCA-LDA) classifier with sixfold cross validation to predict which of 13 different tone frequencies were presented. Although the noise in the Neural Matrix arrays was high, the impact on neural signal acquisition was minimal. The averaged single-trial decoding accuracy was 68.72% (chance, 7.69%) (Fig. 2G). This decoding accuracy was consistent with decoding rates for similar surgical and anesthetic preparations using passive faradaic electrode arrays recorded with low-noise Intan amplifiers (<2.4 μVrms) (15, 16). Signals collected using the Neural Matrix closely matched those obtained from traditional passive arrays (fig. S3).

Although this study was not designed to determine the required spatial sampling resolution to fully capture the detail of the μECoG signal, we evaluated auditory tone decoding accuracy and error

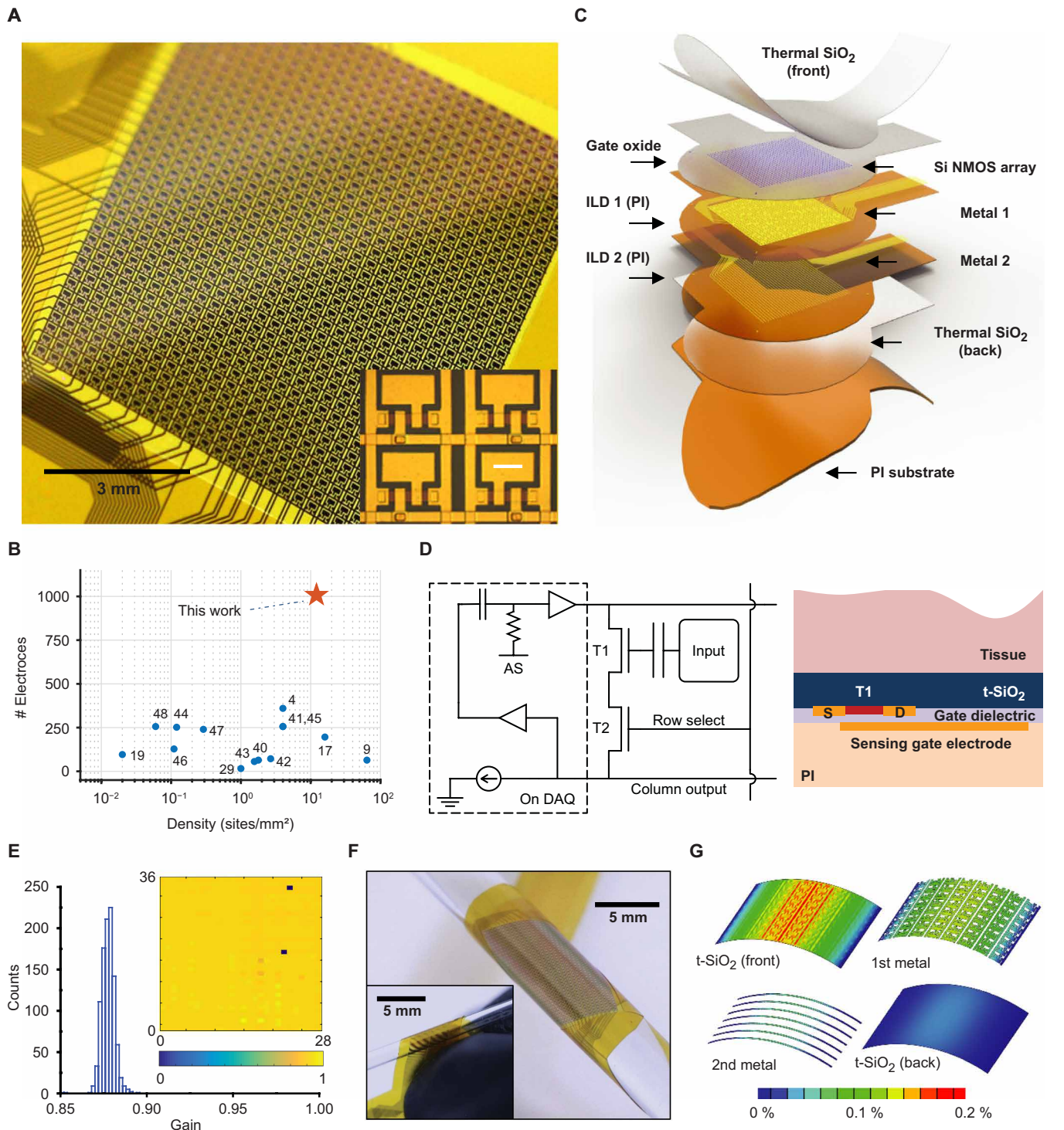


**Fig. 1. The Neural Matrix: A flexible, actively multiplexed electrode array for high-resolution and long-term  $\mu$ ECoG.** (A) Photograph of 1008-ch Neural Matrix array. Inset: Each electrode is connected to a unit cell consisting of two flexible silicon transistors. Scale bar, 100  $\mu$ m. (B) Comparison between this work (kilo-scale device) and other  $\mu$ ECoG studies (blue dots; references listed in table S1). (C) Exploded-view illustration highlighting the key functional layers of a capacitively coupled, flexible neural sensing system with an ultrathin layer of thermally grown silicon dioxide as the encapsulant for chronic operation. (D) Left: Schematic circuit diagram of a single unit cell with two matched transistors for local signal amplification and multiplexing, with active shielding circuit on the DAQ. AS denotes the adjustable active shield bias voltage. Right: Schematic cross section of transistor with capacitive input from adjacent tissue through the thermal  $\text{SiO}_2$  layer. (E) Histogram summary of gain values determined from all 1008 sensors of a representative device. Inset: The spatial distribution of the gain. (F) Image of electrode array bent around cylindrical tubes with radii of 2.5 (main) and 1.25 mm (inset). (G) Computed distribution of bending-induced strains (radius of curvature, 2.5 mm) in four layers of the system ( $\text{SiO}_2$  biointerface layer, first and second metal interconnect layers, and backside-encapsulating  $\text{SiO}_2$  layer) shows strains well below the fracture limit of each material.

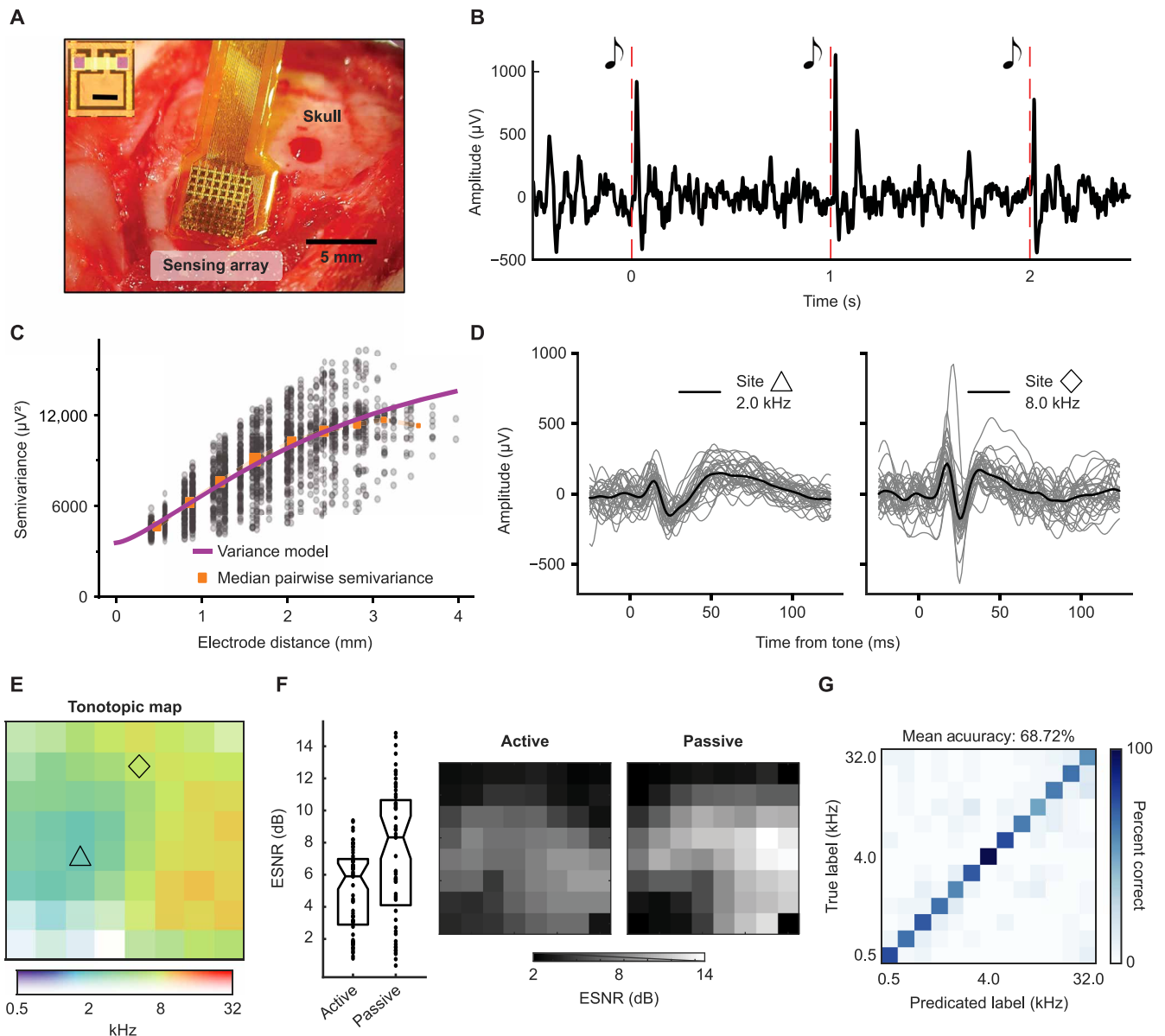


**Fig. 2. Acute experiment demonstrating the capacitive sensing scheme.** (A) The 64-ch Neural Matrix array was acutely implanted epidurally over rat auditory cortex. Field potentials were recorded during a pseudorandomized presentation of tone pips ranging from 0.5 to 32 kHz. Inset: Photograph of a single cell. Scale bar, 150  $\mu\text{m}$ . (B) Three seconds of example raw click-evoked auditory responses from a channel from Neural Matrix array in an acute setup. Raw data were bandpass filtered (2 to 100 Hz). The vertical red dashed line indicates the time when a broadband click sound was presented. (C) Spatial semivariogram analysis measured the dissimilarity of signals as a function of distance and indicated a spatially varying random field. Each gray dot represents the estimates of variance in pairwise differences between electrodes. Variance for each pair was calculated from the baseline signals during the interstimulus period, using samples taken every 50 ms to reduce temporal autocorrelation. (D) Mean and single-trial tone-evoked responses are shown for the best-tuned frequency at two sites on the array separated by  $\sim 1.44$  mm. The selected sites (marked triangle and diamond) are labeled in (E). (E) Tonotopic map predicted from each channel's tuning curve. The best frequency of each channel was determined by mapping each tuning curve's center of mass. Color of each channel indicated the best frequency of the pure-tone sound stimuli. (F) Sensitivity to tone stimuli was measured using ESNR. (G) Confusion matrix showing the prediction versus true label hit rate of each pure-tone sound stimuli. Tone frequencies were predicted using trial response potentials with a mean accuracy of 68.72% (chance, 7.69%).

after subsampling electrodes. To vary the spatial resolution, we used Poisson disc sampling (18) with a minimum of four electrodes to approximately maintain spatial coverage but vary the average spatial resolution. We binned accuracy and error values by the number of electrodes (4 to 7, 8 to 11, and so on;  $n \geq 15$  samplings per bin) and compared mean values to 95% accuracy and 105% error results

from the full set of electrodes. Many subsets with four to seven electrodes had relative decoding scores of more than half the maximum accuracy and less than twice the minimum error, similar to previous sensory decoding results (19). The smallest group of electrodes with accuracy above 95% of the reference value was 56 to 59 electrodes for rat B and 52 to 55 electrodes for rat 1 ( $P < 0.05$ ; one-sided

*t* test with Bonferroni correction for 15 groups). The last group of electrodes with error lower than 105% of the full data set error was 60 to 63 electrodes for both rats ( $P < 0.05$ ; one-sided *t* test with Bonferroni correction). We also compared auditory tone decoding scores for fixed-density, square subgrids with sizes of  $2 \times 2$  to  $7 \times 7$ . Small-area subgrids ( $<4 \times 4$  in rat 1 and  $<5 \times 5$  in rat B) offered worse scores compared with electrode subsets with similar counts ( $\pm 1$  electrode) but larger coverage. Thus, both high density and wide coverage were required to maintain high decoding accuracy in these experiments (fig. S4).

### Long-term reliability in rats

To demonstrate the long-term reliability of the arrays, we implanted t-SiO<sub>2</sub>-encapsulated  $8 \times 8$  array devices chronically in five adult Sprague-Dawley rats. The longevity of a chronic implant typically depends on the speed of biofluid ingress. For an implantable system with integrated active electronics, biofluid penetration not only damages the recording capability of the device but also may induce unsafe leakage currents that can damage the brain. We designed our data acquisition system (DAQ) to continuously monitor for leakage current throughout all recording sessions. Leakage current remained at the noise floor of the recording system and well below our safety threshold of  $1 \mu\text{A}$  for more than a year in all implants but one (4 of 5; Fig. 3A).

During this chronic experiment, recordings were collected at intervals of 1 to 2 weeks, with a mean implant duration of 287 days (min, 63; max, 435). Only one implant was terminated early because of irregular leakage current readings (Fig. 3A); later analyses determined that the leakage current was due to debris in the implant connector. The endpoints of the remaining four implants were caused by sudden and irreparable loss of the headcap structure. When it was possible to retrieve the electrode array, we used focused ion beam (FIB) milling and cross-sectional scanning electron microscopy to measure the remaining thickness of the t-SiO<sub>2</sub> encapsulation (fig. S5). The average in vivo dissolution rate was  $\sim 0.46 \text{ nm/day}$ , projecting a life span of  $\sim 6$  years for  $1\text{-}\mu\text{m}$  t-SiO<sub>2</sub>.

Neural signals were successfully recorded through the t-SiO<sub>2</sub> encapsulation for implant durations of over 1 year. We recorded both tone- and click-evoked responses during each recording session. In click-evoked responses, the median ESNR was low (0.46 dB mean), but remained above 0 dB each week over the course of a year (Fig. 3B). We also calculated the percentage of channels with significant ESNR [ $P < 0.05$ , max-signal-to-noise ratio (SNR) permutation test] each week, measured using a response-baseline permutation procedure (16). In aggregate, electrodes displayed significant ESNR ( $P < 0.05$ ) 42.7% of the time (2983 of 6993 electrode sessions) (Fig. 3B). An example of the average evoked responses that remained distinct from the average baseline exceeding 1 year of implant duration is shown in Fig. 3C.

The frequencies of auditory tones were predicted using the same linear classification scheme as used in the acute experiment. Single-trial tone decoding error remained better than chance in all animals throughout the implant duration (Fig. 3D). Tone-evoked responses were also clearly visible throughout (movies S1 and S2). Examples of spatial semivariograms observed at multiple points for two implants are shown in Fig. 3E to demonstrate that noise power (the vertical offset of the semivariogram) and local field potential (LFP) power (the height of the semivariance curve) remained consistent. A locally varying signal process remained observable and had nearly constant root mean square (RMS) power over the implant duration, similar to implants of passive, faradaic electrodes over the same time

period (Fig. 3F). Sufficiently large spatial heterogeneity to make these observations was only present in two rats. In a separate preliminary experiment, clear bouts of high-amplitude, rhythmic (6 to 9 Hz), spontaneous potentials (SPs) were consistently observed from the whisker somatosensory cortex (S1) for over 4 months (fig. S6).

### Scalability of neural matrix arrays in NHPs

To demonstrate scalability, we fabricated kiloscale Neural Matrix arrays and implanted them in NHPs. Devices and implants were optimized efficiently using iterative testing (fig. S7). We tested the arrays by implanting them over sensorimotor cortices (Fig. 4A) of four awake monkeys using an artificial dura-based ECoG implant (20) (fig. S7E). Numerous iterations in the design and packaging of the device across four animals were necessary to optimize the device for in vivo awake behaving monkey experiments (see Materials and Methods). Arrays were embedded into an artificial dura, which was then implanted into a recording chamber (fig. S7F). Initial testing demonstrated that microscopic cracks introduced by handling the array and cables shortened device lifetimes. We therefore designed an insertion strategy and tool to place the device subdurally and minimize device handling during implantation (see Materials and Methods). In addition, the electrode interconnection cables exiting the array in the artificial dura were bent  $90^\circ$  with a bending radius  $<2 \text{ mm}$ . To enhance the robustness at the interconnect cable area, a protection layer of  $12.5 \mu\text{m}$  of polyimide (PI) was added to the top surface of the array cable. The additional PI shifted the neutral mechanical plane closer to the front t-SiO<sub>2</sub> barrier, reducing induced strain. Consequently, the molded array retained its functionality and performance without any degradation during implantation. The implanted array covered premotor, primary motor, and primary sensory cortices (Fig. 4A). Detailed information on the implantation strategy can be found in Materials and Methods and in fig. S7.

We performed our first behavioral kilo-scale Neural Matrix recordings by presenting repeatable full-field visual stimuli to evoke similar responses across sensorimotor cortices. We found clear visual evoked potentials (Fig. 4B) that were consistent in amplitude across the electrode array (Fig. 4C) and showed a propagating wave moving from sensory to motor cortices (fig. S8 and movie S3). We then recorded from the Neural Matrix array while the animal performed a delayed-reach task to seven peripheral targets (center-out design). The Neural Matrix array successfully revealed the spatial-temporal organization of motor processing. Broadband signals showed movement-related activity, with motor evoked potentials (MEPs) across the array (Fig. 4D). MEPs also showed clear spatial organization across the array that varied with the direction of the arm movement reach (Fig. 4, E and F and movie S4). We further examined movement-related signals using spectral decomposition. We found low-frequency, motor-related potentials in the 0.5- to 2-Hz band with direction tuning evident across multiple time points during movement (Fig. 4G). The degree of tuning varied across both time and sites within the array. To examine the spatial organization of direction tuning, we fit a cosine tuning model to each electrode across different times within the trial (Fig. 4, H and I). During movement planning (Fig. 4H), tuning was weaker and more spatially localized to the arm areas of premotor cortex compared with the tuning observed during movement execution (Fig. 4I), which was widely distributed across the sensorimotor cortices. Across the device, we computed the first time window at which the cosine tuning model described a statistically significant ( $P < 0.05$  for four consecutive time intervals) amount of data variance (Fig. 4J),

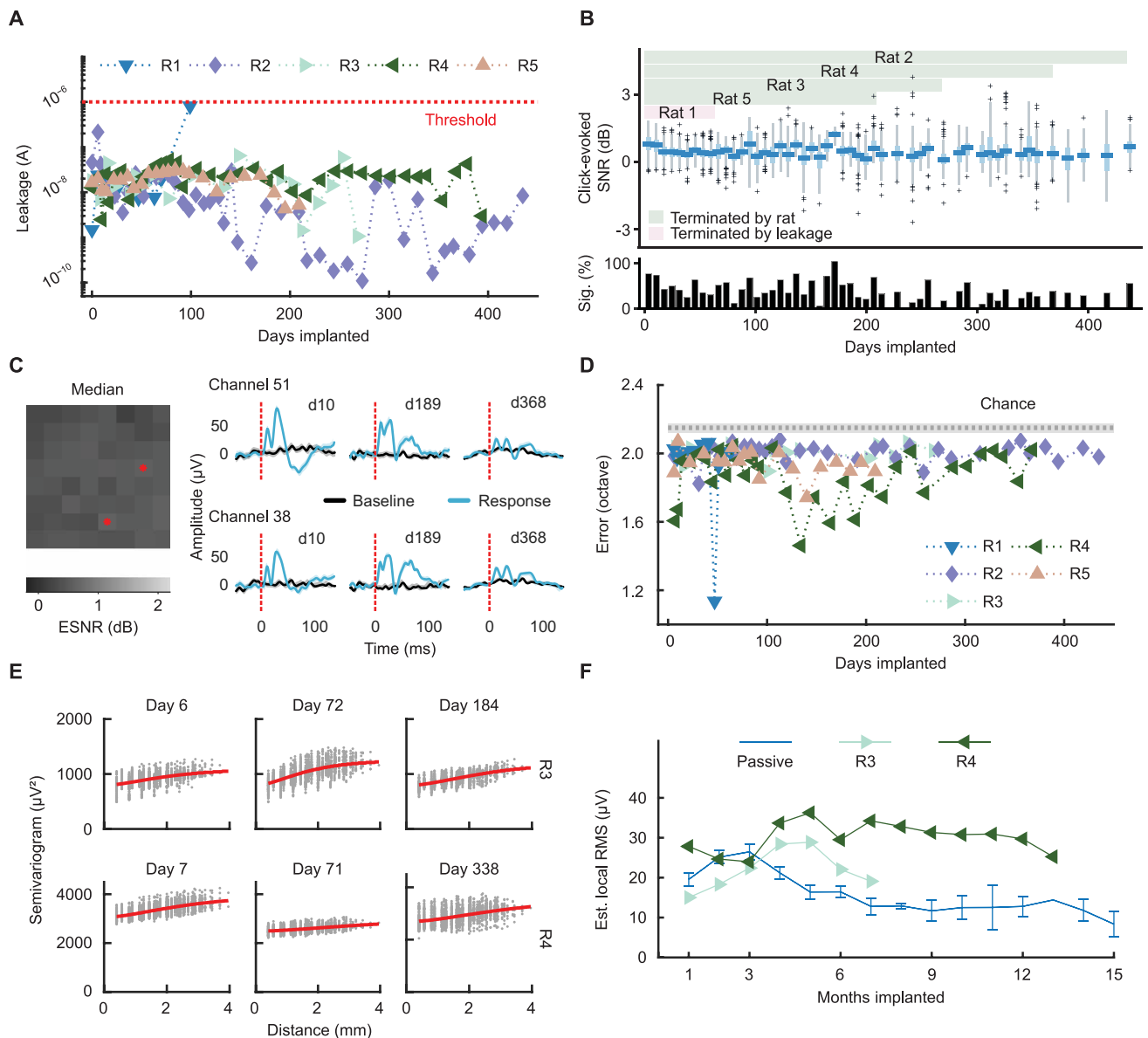


**Fig. 3. Long-term implantation of Neural Matrix arrays.** (A) Leakage current was continuously measured throughout all recording sessions and remained below the cutoff of 1  $\mu$ A in all implants except in rat 1 (R1). (B) Click-evoked responses were measured during each recording session. Recordings from each animal and week were binned together and are shown in box plots (median bin size, 151 electrode sessions; min, 54; max, 445). Top horizontal bars indicate the implant duration for each animal. The bar plot at the bottom shows the percentage of channels in each week with significant ESNR ( $P < 0.05$ , max-SNR permutation test). (C) Example click responses (blue) and baseline potentials (black) recorded from rat 4 (R4) at three points in the implantation history show average evoked responses that remained distinct from the average baseline exceeding 1 year of implant duration. The median ESNR across recording sessions is mapped per electrode. (D) Single-trial tone decoding error was measured, in octaves, in each recording session. Decoding remained above chance (2.15 octaves) in all animals throughout the implant duration. (E) Example semivariograms from two rats (R3 and R4) at early, middle, and late implant time points. Semivariance analysis was performed for each recording session to validate a spatially varying process and to track the noise power (the vertical offset of the semivariogram) and local field potential power (indicated by the height of the semivariance curve). (F) Average total signal variation was measured longitudinally with root-mean-square voltage calculated on the voltage time series. Field power calculated from semivariogram analysis (in microvolt units) is shown.

which revealed how the timing of tuning progressed from premotor to primary motor and to primary sensory cortices. These Neural Matrix array recordings resolved the large-scale progression of movement selectivity at high resolution across sensorimotor cortices during transformation from movement planning to execution.

To compare the Neural Matrix to more traditional intracortical electrodes, we simultaneously measured  $\mu$ ECoG signals recorded from

the surface using passive electrodes that included holes in the array and intracortical electrodes (including spiking and LFP signals) from varying depths in an anesthetized NHP and analyzed correlation and coherence between these signals (fig. S9). Correlations between  $\mu$ ECoG and intracortical signals were strongest near the surface; however,  $\mu$ ECoG also showed focal correlation with LFPs at 0.75-mm depth (fig. S9D). Further,  $\mu$ ECoG signals showed strong coherence

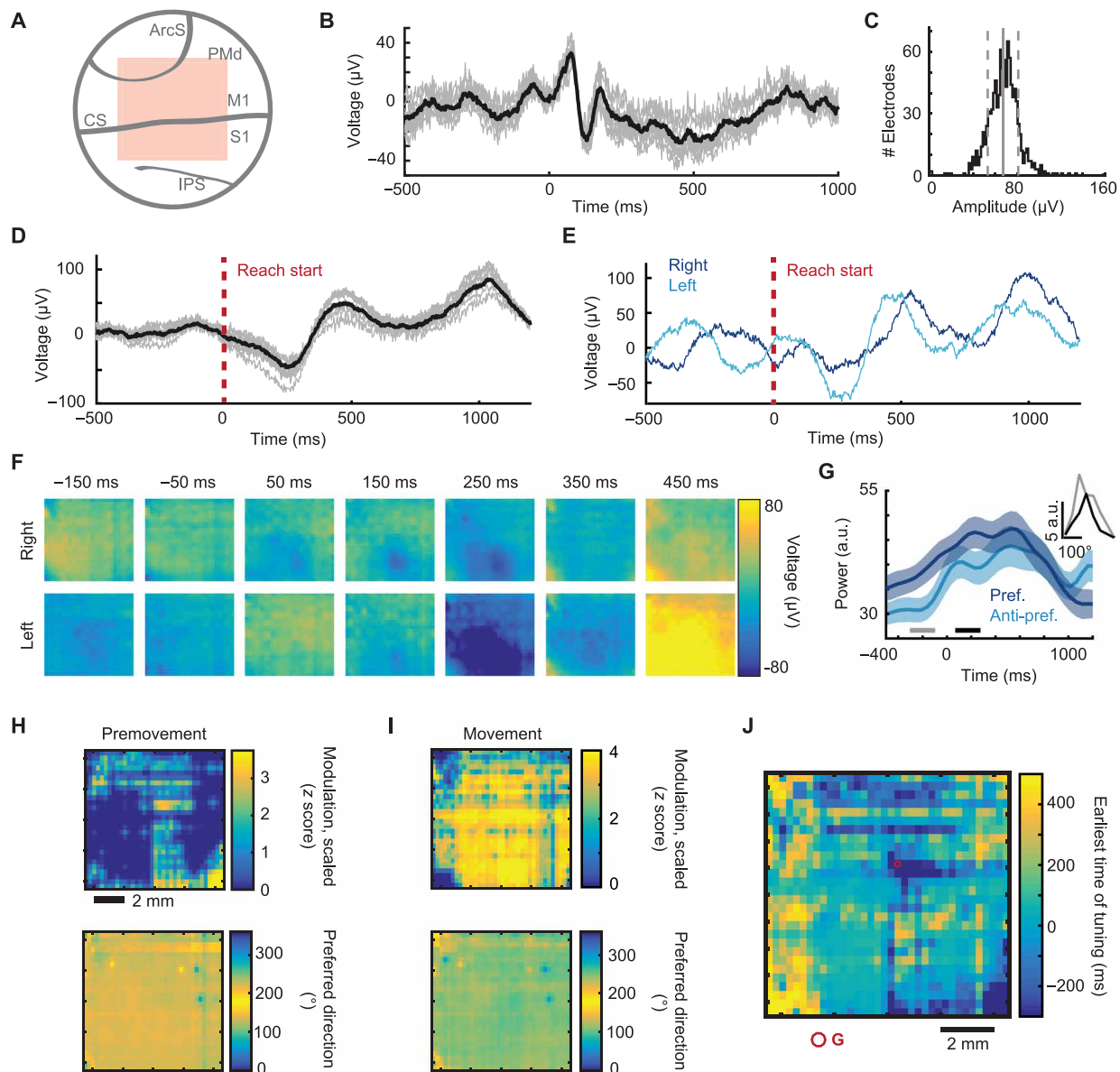


**Fig. 4. Kilo-scale, multibrain region recordings in NHPs.** (A) Schematic representation of electrode array placement on the cortical surface. The circle represents the full implant area; the shaded orange area denotes the region of electrode contacts. The recording area spans premotor, primary motor, and primary sensory cortices. ArcS, arcuate sulcus; CS, central sulcus; IPS, intraparietal sulcus; PMd, dorsal premotor cortex; M1, primary motor cortex; S1, primary sensory cortex. (B) Evoked visual potentials (broadband), triggered at the time of visual stimulus onset, computed across all visual stimulation trials. The black trace shows the mean across all 1008 electrodes; gray traces show examples for 10 randomly selected electrodes. (C) Distribution of visual evoked potential amplitudes across the array (black); solid gray line shows mean, and dashed gray shows  $\pm\sigma$  interval. (D) Evoked movement potentials (broadband), triggered at the time of movement onset, computed across all reach trials. Format as in (B). (E) Evoked movement potentials as in (D), now separated by movement directions. Traces represent the mean across all 1008 electrodes. Two of the seven movement directions are shown (dark blue, rightward reach; light blue, leftward reach). (F) Spatial maps of evoked movement potentials, separated by movement directions (top row, rightward reach; bottom row, leftward reach) over time during movement. Full temporal evolution shown in movie S4. (G) Direction tuning in the 0.5- to 2-Hz band for an example electrode. Average power across trials, separated by reach direction, for two directions (preferred and antipreferred directions during reaching). Solid lines show the trial mean, shaded regions represent the standard error. Inset shows the average power as a function of movement direction for two different time windows (premovement [−300 ms, −100 ms] in gray; movement [100 ms, 300 ms] in black). (H) Spatial map of cosine tuning parameters across the electrode array for the premovement period [−300 ms, −100 ms]. Scaled modulation depth (top, see Materials and Methods) and preferred direction (bottom) show focal and weak tuning centered around the arm area of the premotor cortex. (I) As in (G) but for the early motor period [100 ms, 300 ms]. Tuning during movement grows to cover large portions of the arm areas of sensorimotor cortices. (J) Spatial map of the time window when directional tuning first became statistically significant ( $P < 0.05$  for four consecutive time intervals) for each electrode reveals a temporal evolution of directional information starting in focal areas of the premotor cortex that then shifts to the primary motor and sensory cortices. Location of the example electrodes from (G) is indicated by the red circle. a.u., arbitrary units.

with LFPs recorded from 0.75 and 1.25 mm within the cortex (fig. S9E). This coherence was spatially specific and substantially reduced in distant  $\mu$ ECoG contacts. Coherence in low-frequency bands (<10 Hz) found to encode movement information was particularly pronounced.  $\mu$ ECoG signals also showed strong coherence with multiunit activity captured from deeper layers of the cortex (1.25 mm) (fig. S11F). Coherence was both spatially specific to nearby electrodes and most pronounced in low-frequency bands (<10 Hz).

## DISCUSSION

Our approach improves on the state-of-the-art in multiple ways: (i) Scaling to over a thousand channels with fewer than 100 external wires was achieved through integration of flexible, active electronics at each electrode contact. (ii) The device is ultrathin (~29  $\mu$ m) to ensure conformal contact with the brain and improve signal longevity. Device longevity was increased by (iii) using t-SiO<sub>2</sub> encapsulation strategies and (iv) changing the method of electrical sensing from faradaic to capacitive. (v) Rapid, iterative in vivo testing in NHPs was enabled by using integrated artificial dura array packaging (20). Moreover, our devices were made using standard silicon fabrication processes. Transitioning our design to commercial fabrication will simultaneously enable increased sensor resolution and larger coverage while producing large quantities of devices at low cost.

These results demonstrate possible solutions to several critical challenges faced by all implantable active electronics in the body. We established methods to achieve safe, robust, and high-performance flexible electronics with in vivo durability projected to be at least 6 years in a scalable design optimized using an iterative testing procedure. The encapsulation scheme could be modified to extend longevity to a human life span by adding an additional 100 nm of HfO<sub>2</sub> (13) or by using a trilayer structure with 50 nm of Parylene C (14) to further slow the dissolution rate.

High-resolution kilo-scale and mega-scale neural interfaces will be increasingly important in the next generation of neural diagnostic (21, 22), therapeutic (23, 24), and prosthetic (25) devices. The iterative testing strategy we present here will enable further device scaling offering powerful insights into brain function. Active devices can sample large areas of the brain at high density, and we anticipate they will be able to resolve multiunit activity from the surface of the brain (9). Our simultaneous analysis of  $\mu$ ECoG and intracortical electrodes suggests that  $\mu$ ECoG may capture signals with strong relationships to intracortical electrodes.  $\mu$ ECoG may also capture spatially specific signals, reflecting LFP and multiunit activity from the upper cortical layers. This suggests the surface activity may provide an excellent signal for neural prosthetic applications.

However, there were some limitations to this work. Scar tissue may be observed under similarly sized electrode arrays when chronically implanted based on prior studies (26). Although we did not perform histology in these experiments, we have implanted similar devices using t-SiO<sub>2</sub> encapsulation in the mouse brain and performed histology at 5 weeks after implant (27). Histopathological evaluation of the images revealed no sign of inflammation, necrosis, or structural abnormalities in the brain, heart, kidney, liver, lung, or spleen, suggesting that Neural Matrix arrays might be safely implanted long term. This will need to be investigated in future studies.

Another limitation to this work was the increased noise in Neural Matrix devices. We suspect that the noise in the Neural Matrix devices was high due to imperfections in transistors manufactured in a univer-

sity cleanroom. We predict that commercial complementary metal-oxide-semiconductor (CMOS) could markedly reduce noise in the device by incorporating higher-quality transistors and local amplification. Leveraging commercial CMOS manufacturing might provide numerous additional benefits for future generations of high-throughput neural interfaces. CMOS will likely enable neural interface systems to scale to millions of electrodes, well beyond what is possible using passive electrodes that are individually wired to remote electronics. CMOS integration will also enable electrical stimulation, amplification, digitization, on-board signal processing and data reduction, and wireless data and power transmission, creating an implantable device where the integrated circuit is the entire system. Although the optimal spatial sampling density for low-frequency neural signals (LFP) is currently unknown, spatial oversampling of lower-frequency LFP will enable additional noise reduction techniques to mitigate the aliased noise introduced by multiplexing at the electrode without low-pass filtering (28).

In summary, we developed an implantable active electrode array, the Neural Matrix, for long-term in vivo use in a preclinical setting with flexible electronics that are scalable in coverage, channel count, and resolution. Neural recordings were stable for over a year of implantation in rodents and showed similar stability to gold contact, faradaic, passive electrodes (16). Our results validate techniques for fabrication and in vivo testing of long-lived, encapsulated active electronics that readily scale to high channel counts, enabling a new generation of flexible neural interfaces for prosthetic and closed-loop therapeutic applications.

## MATERIALS AND METHODS

### Study design

To choose the spacing between electrodes in the design of our Neural Matrix electrodes, we considered recent studies that compared electrode correlation or coherence by electrode pitch. These studies suggest that the spatial correlation of  $\mu$ ECoG varies from submillimeter to a few millimeters depending on the recording location (epidural or subdural) and whether the animal is awake (15). The spatial correlation is also highly dependent on the frequency band (29, 30). Therefore, we wanted to sample densely (250- $\mu$ m pitch in NHPs and 400- $\mu$ m pitch in rats) to be able to resolve fine features in the  $\mu$ ECoG signal.

We chose to focus our experiments on LFP signals mainly because of limitations of the DAQ. The DAQ was not able to sample fast enough to capture spiking activity from the surface of the brain. Further, we can readily compare LFP signals from auditory cortex to prior work (15, 16). In contrast, spiking activity from the surface of the brain has not yet been sufficiently described in the literature to be useful as a benchmark signal for neural technologies. Therefore, we chose to bandpass filter the data between 2 and 100 Hz to study the LFP activity captured by the arrays.

The behavioral experiments in NHP were designed to test the ability of the device to measure neural responses to sensory and motor stimuli and resolve motor cortical tuning. For the visual response task, we presented the visual stimulus a sufficient number of times to resolve a motor cortical visual evoked potential. For the center-out task, we randomly interleaved trial conditions requiring movements to different targets and collected data until the monkey decided to stop performing the task.

We designed our rat studies to test the longevity of the Neural Matrix devices for as long as possible. We chose not to euthanize the

animals at specific endpoints, as would be required to obtain histology. Instead, we left the devices implanted as long as possible to assess their longevity. Each implant ended when the rat's headcap became detached, causing irreparable damage to the implant. Seven rats (five chronic and two acute) and four NHPs were implanted in this study.

### Capacitive sensing

Each unit cell contained two n-channel MOSFETs (metal oxide semiconductor field-effect transistors). The source-follower transistor buffered the capacitively sensed neural potential, and the switch transistor provided multiplexing between electrodes in the same column. The large area of the electrode provided a sensing capacitance roughly three times larger than the gate capacitance of the transistor. The sensing electrodes were  $100 \times 180$  and  $195 \times 270 \mu\text{m}^2$  for devices used in NHP and rat studies, respectively. From the thin film capacitance equation,  $C = \epsilon_r \epsilon_0 A/t$ , where  $\epsilon_r$  is the relative permittivity,  $\epsilon_0$  is the vacuum permittivity,  $A$  is the area, and  $t$  is the thickness of the dielectric,  $C_{\text{sensing NHP}} = 3.3C_{\text{gate NHP}}$  and  $C_{\text{sensing rat}} = 4.9C_{\text{gate rat}}$ . The input capacitance driving the channel in the sensing transistors for NHP and rat model were then  $0.77C_{\text{gate NHP}}$  and  $0.83C_{\text{gate rat}}$ , respectively, from combining sensing and gate capacitance in series. The effective capacitance of the electrode gate was further reduced by active shielding, ensuring unity gain from the sensing transistor.

Characterization from a passive electrode array (fig. S10) using the same capacitive sensing through  $\sim 1 \mu\text{m}$  of t-SiO<sub>2</sub> yielded an estimated capacitance of  $\sim 2$  and  $\sim 0.7$  pF and corresponding electrode impedance of  $\sim 80$  and  $\sim 230$  megohms at 1 kHz for the rat and NHP electrodes, respectively. These high electrode impedances were converted to substantially lower output impedances by the current gain of the integrated buffer amplifier at each electrode.

### Mechanical analysis

The strain distribution in the neural sensing array under pure bending was modeled using FEA. The device was pressed conformally onto a rigid cylinder with a predefined radius. Three-dimensional solid elements (C3D8R in Abaqus finite element software) were used for thicker layers including the Kapton layer, PDMS (polydimethylsiloxane) layer, PI layer, and top thermal silicon oxide layer, whereas shell elements (S4R) were used for thin Au layers. For a 2.5-mm bending radius at the sensing area (bottom surface), the maximum strain was  $\sim 0.2\%$  in the top thermal oxide layer,  $0.17\%$  in the first metal layer, and  $0.1\%$  in the second metal layer.

In the NHP experiment, the DAQ design was scaled up to record 1008 channels by using more PXI-6289 cards. An effective final sampling rate of 434 Hz per electrode channel was achieved. The system diagram for NHP experiments are shown in fig. S12.

### Awake recording (rat)

All chronically implanted rats were recorded while freely behaving in a sound-attenuated chamber. The equipment and experimental stimuli were the same as described in the rat acute experiment. The first recording sessions were performed 7 days after surgery. Each rat was recorded initially every week and then later every 2 weeks. Leakage current was continuously monitored during all recordings to ensure safety.

### Data analysis (preprocessing/spatial denoising)

$\mu\text{ECoG}$  field recordings were bandpass filtered from 2 to 100 Hz using third-order Butterworth filters. Tone- and click-evoked epochs

were further processed with a heuristic hard-threshold singular value decomposition (SVD) denoising for multichannel data (31). Both the neural field signal and the electrode/electronic noise are autocorrelated signals, causing the SNR to vary with frequency. To adapt to varying SNR, we applied the hard-threshold SVD denoising to sub-band signals using a tight-frame tunable-Q wavelet transform (TQWT), with 10 log-spaced, redundant frequency bands in addition to a low-pass residual (32). Sub-band wavelet coefficients were computed for a multi-channel matrix composed of concatenated evoked responses. The denoised coefficients were then reconstructed to full band with the inverse TQWT.

### Evoked signal-to-noise ratio

We measured detectability of evoked responses using an ESNR metric of poststimulus versus prestimulus time series (16). Evoked-signal power in ESNR was computed using the average Mahalanobis distance of poststimulus vectors from a large sample of baseline vectors. This distance can be interpreted as measuring the improbability of a response vector arising from the same stochastic process as the baseline vectors. The ratio was normalized by the average Mahalanobis distance of the individual prestimulus baseline vectors. We pooled all trials when measuring click-evoked SNR, but the tone-evoked SNR was measured using only the maximum-distance tone (and a matching sample of the largest percentile of baseline distances).

### Tone decoding

We used the linear classifier described in (15, 33) to predict tones given array responses. Response covariates were concatenated from the field potential at each channel, bandpass filtered from 2 to 100 Hz, and windowed from 5 to 80 ms following each tone presentation. A channel was fully omitted from the classifier if more than 5% of its responses were outlying. For channels with a lower number of outlying responses, such samples were imputed from the surrounding array channels using image in-painting that iteratively filled masked pixels based on points bordering the missing regions. Tone decoding was summarized by accuracy (the proportion of successfully classified trials) and the average error of classification, measured in octave difference between the predicted and true tone.

### In vivo recording (NHP)

Packaging devices to enable rapid, iterative testing in awake, behaving monkeys trained to perform behavioral tasks let us optimize the devices. Subdural cortical surface electrodes are typically implanted onto the cortical surface, and the electrode interconnection cable containing the electrical activity percutaneously exits the implantation site to an external connector (fig. S7A). In chronic implants, devices are minimally packaged (fig. S7B), requiring manual probe placement and cable routing during surgery. Because the Neural Matrix arrays were actively powered, damage to the electrode interconnect cable leads to leak currents and device failure. Device testing cycles with a traditional implant technique (fig. S7C) are slow and nonmodular. Each test outcome takes on the order of months because it requires preparing a new animal, new surgical implantation, and post-op recovery before awake behavioral recordings can occur. Furthermore, all aspects of the implant—device, placement, and packaging—change on each iteration, making careful isolation of failure modes difficult. We developed a chamber-based implant and device packaging system (fig. S7, D to F). Probes are placed by packaging them into an artificial dura, which is nonsurgically replaceable. Cable routing is specified by this packaging (fig. S7, D and E) and chamber geometry (fig. S7F)

and is therefore reproducible and controlled. Sterile implant sealing is achieved using chamber hardware (fig. S7F), providing reversible and mechanically reproducible seals. This innovation provides both rapid and modular test cycles (fig. S7G) by separating the surgical hardware implantation from probe-specific testing. Animal preparation (training and surgical implants, which take months) is separate from device placement and testing, producing test cycles from new device to behavioral recordings on the order of days. The chamber-based approach affords precision and control in device placement and packaging, which allows modular testing of the device, its placement, and packaging. Last, this strategy allows more test cycles to be performed within the same animal and surgical site, providing a way to ethically reduce the number of animals needed for a study. For our iterative testing and recordings, we first implanted a recording chamber in which the dura was replaced with an artificial dura. We then tested individual devices by replacing the artificial dura with another that contained an embedded ECoG array (20). The artificial dura was replaced with the one containing the embedded device immediately before the recordings.

Several revisions were necessary to avoid postimplantation damage to the electrode interconnect cable. We made changes in the artificial dura to avoid stress on the arms where they bent within the mold. We made refinements to the implantation procedure to minimize array handling by designing a custom insertion tool. With the insertion tool, the array could be implanted by simply placing it onto the cortical surface without the need to make additional adjustments. Last, we made changes to the chamber system to avoid stress on the arms when sealing the implant site after implantation. Over 20 iterations in the design of the device and packaging across four animals were necessary to optimize the device for in vivo awake behaving monkey experiments.

Having optimized the kilo-scale Neural Matrix array and packaging, we successfully recorded neural activity in the third animal performing two behavioral tasks. In the visual task, we presented full-field visual stimuli, which the animal viewed passively. Full-field visual stimulation was performed by illuminating the task display for 150 ms with randomly spaced intertrial intervals (400 to 1000 ms). Next, in a motor task, the animal performed the delayed center-out reach task on a touch screen. The animal touched an initial central target for a short baseline interval (400 to 600 ms), after which one of seven possible peripheral targets appeared on the screen (circular arrangement with 45° spacing, excluding the bottom-most target). After an instructed delay (250 to 750 ms), the central target disappeared, cueing the animal to reach to the peripheral visual target. Successfully acquiring the peripheral target resulted in a liquid reward. Target directions were presented in a pseudorandom order with balanced distributions of successful target acquisitions to all targets. We define reach onset as the time at which the animal lifts its hand off the screen to begin moving to the peripheral target. Figure 4 presents data from a behavioral session in which we presented full-field visual stimuli 581 times and the monkey performed 412 successful reach trials.

### Data preprocessing (NHP)

Raw broadband data revealed periodic physiological artifacts, which we denoised using a mode decomposition procedure (34) followed by spectral harmonic suppression. We estimated the empirical modes using PCA. The spectra of the individual modes revealed evidence of power in excess of a smooth background. We suppressed the ex-

cess power by modeling the raw signal as a sinusoid with variable amplitude, phase, and frequency within  $2.5 \pm 1$ ,  $5 \pm 1$ , and  $7 \pm 1$  Hz. We fit the sinusoid every 5 s (*F* test). We then subtracted the modeled time series from the empirical modes. The results of the procedure were validated by comparing the empirical mode spectra before and after denoising and confirming excess power was no longer present. We then transformed the data back into the original [space, time] coordinates for further analysis.

### Data analysis (NHP)

All analyses were performed with trial-aligned data aligned to the time of reach start. Neural activity was mean subtracted on a trial-by-trial basis for each electrode to remove dc offsets. Movement-evoked potentials were computed by averaging trial-aligned broadband signals across trials. Spectral analyses were done by computing power in the 0.5- to 2-Hz band with multitaper spectral estimation (1-s window, 2-Hz frequency smoothing window, and 50-ms step size). Direction tuning was computed by relating the mean power with movement direction, similar to spiking models used in motor cortex (35). Each contact's power (*f*) was fit to a cosine direction tuning function:

$$f = B_1 \cos(\theta) + B_2 \sin(\theta) + B_3$$

where  $\theta$  represents the reaching angle, and  $B_1$ ,  $B_2$ , and  $B_3$  are linear constants. A modulation depth (MD) and preferred direction (PD) are then defined as  $MD = \sqrt{B_1^2 + B_2^2}$  and  $PD = \arctan(B_2/B_1)$ , resolved to the correct quadrant. Tuning parameters were estimated using the average power in a given time window, which was varied (see Fig. 4, F to H). Reach angle was determined by the reach target location. Tuning parameters, regression coefficients ( $R^2$ ), and statistical significance (*P* value) of model fits were estimated via linear regression (MATLAB, MathWorks Inc.). For map visualization (Fig. 4, G and H), MDs were scaled by a weighting factor proportional to the significance value of the fit. Each electrode MD was scaled by a weight *w*, which was related to *P* values via a logistical function that was approximately 1 small *P* value and rapidly decayed to zero for less significant fits:  $w = 1/(1 + e^{-k(p_0 - p)})$  with constants *k* and  $p_0$  set to 100 and 0.08, respectively. The timing of the first tuning was computed by fitting a cosine tuning model with a sliding window (200-ms window length, 25-ms step size) and finding the first time when at least four consecutive windows had *P* values <0.05. The reported time represents the start of the 200-ms window. All spatial maps were smoothed using a Gaussian filter with 0.6-pixel SD.

### Statistical analysis

In rodent experiments, analysis of spatial variation (semivariance) of  $\mu$ ECoG field potential was computed by one-half the sample variance of pairwise electrode differences. A covariance kernel including noise and "local" field variance parameters was fit to semivariance clouds using nonlinear least squares. Local RMS voltage was the square root of the estimated field variance parameter. To assess significance of ESNR values under multiple comparisons, we used permutation testing. Under the null hypothesis that evoked and baseline trials were interchangeable, we computed the maximum ratio across electrodes ("max-SNR") for 5000 permutations of evoked/baseline labels per recording. True ESNR values above the 0.95 quantile of a max-SNR sample corresponded to significance at  $P < 0.05$ .

All NHP data that are not single trial are shown as a mean with confidence intervals (CIs) indicating standard errors. Statistical analysis

of directional tuning parameters,  $R^2$ , and statistical significance ( $P$  value) of model fits were estimated via linear regression. The timing of first tuning was calculated the first time when at least four consecutive windowed regressions were found to be significant at an alpha value of 0.05.

## SUPPLEMENTARY MATERIALS

stm.sciencemag.org/cgi/content/full/12/538/eaay4682/DC1

Materials and Methods

Fig. S1. Design and characterization of the Neural Matrix arrays.

Fig. S2. Semivariogram of passive electrode and noise analysis of the active Neural Matrix electrode array.

Fig. S3. Direct comparison of Neural Matrix and passive array in rat.

Fig. S4. Auditory classification accuracy with varying spatial resolutions.

Fig. S5. FIB measurement of t-SiO<sub>2</sub> thickness postimplantation.

Fig. S6. Stable recording of SPs.

Fig. S7. Chamber-free and chamber-based neurotechnology device testing approaches.

Fig. S8. Detailed spatiotemporal pattern recorded by the kiloscale Neural Matrix array.

Fig. S9. Comparison of  $\mu$ ECoG and intracortical recordings.

Fig. S10. Characterization of a passive capacitive electrode array.

Fig. S11. DAQ for rat experiment.

Fig. S12. DAQ for kiloscale Neural Matrix array.

Table S1.  $\mu$ ECoG comparison table.

Movie S1. Tone-evoked spatiotemporal patterns from rat 4 at day 7 of implantation.

Movie S2. Tone-evoked spatiotemporal patterns from rat 4 after 1 year of implantation.

Movie S3. High-resolution spatiotemporal patterns recorded using kiloscale Neural Matrix in NHP.

Movie S4. Motor-evoked responses from an NHP reaching left and right.

References (36–48)

[View/request a protocol for this paper from Bio-protocol.](#)

## REFERENCES AND NOTES

- E. F. Chang, Towards large-scale, human-based, mesoscopic neurotechnologies. *Neuron* **86**, 68–78 (2015).
- D. Tsai, D. Sawyer, A. Bradd, R. Yuste, K. L. Shepard, A very large-scale microelectrode array for cellular-resolution electrophysiology. *Nat. Commun.* **8**, 1802 (2017).
- J. J. Jun, N. A. Steinmetz, J. H. Siegle, D. J. Denman, M. Bauza, B. Barbarits, A. K. Lee, C. A. Anastassiou, A. Andrei, Ç. Aydin, M. Barbic, T. J. Blanche, V. Bonin, J. Couto, B. Dutta, S. L. Gratiy, D. A. Gutnisky, M. Häusser, B. Karsh, P. Ledochowitsch, C. M. Lopez, C. Mitelut, S. Musa, M. Okun, M. Pachitariu, J. Putzeys, P. D. Rich, C. Rossant, W.-I. Sun, K. Svoboda, M. Carandini, K. D. Harris, C. Koch, J. O'Keefe, T. D. Harris, Fully integrated silicon probes for high-density recording of neural activity. *Nature* **551**, 232–236 (2017).
- J. Viventi, D.-H. Kim, L. Vigeland, E. S. Frechette, J. A. Blanco, Y.-S. Kim, A. E. Avrin, V. R. Tiruvadi, S.-W. Hwang, A. C. Vanleer, D. F. Wulsin, K. Davis, C. E. Gelber, L. Palmer, J. Van der Spiegel, J. Wu, J. Xiao, Y. Huang, D. Contreras, J. A. Rogers, B. Litt, Flexible, foldable, actively multiplexed, high-density electrode array for mapping brain activity in vivo. *Nat. Neurosci.* **14**, 1599–1605 (2011).
- H. Fang, J. Zhao, K. J. Yu, E. Song, A. B. Farimani, C.-H. Chiang, X. Jin, Y. Xue, D. Xu, W. Du, K. J. Seo, Y. Zhong, Z. Yang, S. M. Won, G. Fang, S. W. Choi, S. Chaudhuri, Y. Huang, M. A. Alam, J. Viventi, N. R. Aluru, J. A. Rogers, Ultrathin, transferred layers of thermally grown silicon dioxide as biofluid barriers for biointegrated flexible electronic systems. *Proc. Natl. Acad. Sci.* **113**, 11682–11687 (2016).
- S. F. Cogan, K. A. Ludwig, C. G. Welle, P. Takmakov, Tissue damage thresholds during therapeutic electrical stimulation. *J. Neural Eng.* **13**, 021001 (2016).
- D. B. McCreery, W. F. Agnew, T. G. H. Yuen, L. Bullara, Charge density and charge per phase as cofactors in neural injury induced by electrical stimulation. *IEEE Trans. Biomed. Eng.* **37**, 996–1001 (1990).
- P. Moshayedi, G. Ng, J. C. F. Kwok, G. S. H. Yeo, C. E. Bryant, J. W. Fawcett, K. Franze, J. Guck, The relationship between glial cell mechanosensitivity and foreign body reactions in the central nervous system. *Biomaterials* **35**, 3919–3925 (2014).
- D. Khodagholy, J. N. Gelinis, T. Thesen, W. Doyle, O. Devinsky, G. G. Malliaras, G. Buzsáki, NeuroGrid: Recording action potentials from the surface of the brain. *Nat. Neurosci.* **18**, 310–315 (2015).
- S. M. Won, E. Song, J. Zhao, J. Li, J. Rivnay, J. A. Rogers, Recent advances in materials, devices, and systems for neural interfaces. *Adv. Mater.* **30**, 1800534 (2018).
- Y. K. Lee, K. J. Yu, Y. Kim, Y. Yoon, Z. Xie, E. Song, H. Luan, X. Feng, Y. Huang, J. A. Rogers, Kinetics and chemistry of hydrolysis of ultrathin, thermally grown layers of silicon oxide as biofluid barriers in flexible electronic systems. *ACS Appl. Mater. Interfaces* **9**, 42633–42638 (2017).
- H. Fang, K. J. Yu, C. Gloschat, Z. Yang, E. Song, C.-H. Chiang, J. Zhao, S. M. Won, S. Xu, M. Trumpis, Y. Zhong, S. W. Han, Y. Xue, D. Xu, S. W. Choi, G. Cauwenberghs, M. Kay, Y. Huang, J. Viventi, I. R. Efimov, J. A. Rogers, Capacitively coupled arrays of multiplexed flexible silicon transistors for long-term cardiac electrophysiology. *Nat. Biomed. Eng.* **1**, 0038 (2017).
- E. Song, Y. K. Lee, R. Li, J. Li, X. Jin, K. J. Yu, Z. Xie, H. Fang, Y. Zhong, H. Du, J. Zhang, G. Fang, Y. Kim, Y. Yoon, M. A. Alam, Y. Mei, Y. Huang, J. A. Rogers, Transferred, ultrathin oxide bilayers as biofluid barriers for flexible electronic implants. *Adv. Funct. Mater.* **28**, 1702284 (2018).
- E. Song, R. Li, X. Jin, H. Du, Y. Huang, J. Zhang, Y. Xia, H. Fang, Y. K. Lee, K. J. Yu, J.-K. Chang, Y. Mei, M. A. Alam, Y. Huang, J. A. Rogers, Ultrathin trilayer assemblies as long-lived barriers against water and ion penetration in flexible bioelectronic systems. *ACS Nano* **12**, 10317–10326 (2018).
- M. Insanally, M. Trumpis, C. Wang, C.-H. Chiang, V. Woods, K. Palopoli-Trojani, S. Bossi, R. C. Froemke, J. Viventi, A low-cost, multiplexed  $\mu$ ECoG system for high-density recordings in freely moving rodents. *J. Neural Eng.* **13**, 026030 (2016).
- V. Woods, M. Trumpis, B. Bent, K. Palopoli-Trojani, C.-H. Chiang, C. Wang, C. Yu, M. N. Insanally, R. C. Froemke, J. Viventi, Long-term recording reliability of liquid crystal polymer  $\mu$ ECoG arrays. *J. Neural Eng.* **15**, 066024 (2018).
- M. A. Escabi, H. L. Read, J. Viventi, D.-H. Kim, N. C. Higgins, D. A. Storace, A. S. K. Liu, A. M. Gifford, J. F. Burke, M. Campisi, Y.-S. Kim, A. E. Avrin, V. D. Spiegel, Jan, Y. Huang, M. Li, J. Wu, J. A. Rogers, B. Litt, Y. E. Cohen, A high-density, high-channel count, multiplexed  $\mu$ ECoG array for auditory-cortex recordings. *J. Neurophysiol.* **112**, 1566–1583 (2014).
- R. Bridson, Fast Poisson disk sampling in arbitrary dimensions, in *SIGGRAPH Sketches* (ACM, San Diego, California, 2007), pp. 22.
- T. Kajiu, K. Doi, M. Yokota, K. Watanabe, M. Inoue, H. Ando, K. Takahashi, F. Yoshida, M. Hirata, T. Suzuki, High spatiotemporal resolution ECoG recording of somatosensory evoked potentials with flexible micro-electrode arrays. *Front. Neural Circuits* **11**, 20 (2017).
- A. L. Orsborn, C. Wang, K. Chiang, M. M. Maharbiz, J. Viventi, B. Pesaran, Semi-chronic chamber system for simultaneous subdural electrocorticography, local field potentials, and spike recordings, paper presented at the 2015 7th International IEEE/EMBS Conference on Neural Engineering (NER), Montpellier, France, 22 to 24 April 2015.
- M. O. Baud, J. K. Kleen, G. K. Anumanchipalli, L. S. Hamilton, Y.-L. Tan, R. Knowlton, E. F. Chang, Unsupervised learning of spatiotemporal interictal discharges in focal epilepsy. *Neurosurgery* **83**, 683–691 (2018).
- S. V. Gliske, Z. T. Irwin, C. Chestek, G. L. Hegeman, B. Brinkmann, O. Sagher, H. J. L. Garton, G. A. Worrell, W. C. Stacey, Variability in the location of high frequency oscillations during prolonged intracranial EEG recordings. *Nat. Commun.* **9**, 2155 (2018).
- V. R. Rao, K. K. Sellers, D. L. Wallace, M. B. Lee, M. Bijanzadeh, O. G. Sani, Y. Yang, M. M. Shanechi, H. E. Dawes, E. F. Chang, Direct electrical stimulation of lateral orbitofrontal cortex acutely improves mood in individuals with symptoms of depression. *Curr. Biol.* **28**, 3893–3902.e4 (2018).
- O. G. Sani, Y. Yang, M. B. Lee, H. E. Dawes, E. F. Chang, M. M. Shanechi, Mood variations decoded from multi-site intracranial human brain activity. *Nat. Biotechnol.* **36**, 954–961 (2018).
- T. Milekovic, A. A. Sarma, D. Bacher, J. D. Simeral, J. Saab, C. Pandarinath, B. L. Sorice, C. Blabe, E. M. Oakley, K. R. Tringale, E. Eskandar, S. S. Cash, J. M. Henderson, K. V. Shenoy, J. P. Donoghue, L. R. Hochberg, Stable long-term BCI-enabled communication in ALS and locked-in syndrome using LFP signals. *J. Neurophysiol.* **120**, 343–360 (2018).
- A. A. Schendel, M. W. Nonte, C. Vokoun, T. J. Richner, S. K. Brodnick, F. Atry, S. Frye, P. Bostrom, R. Pashaie, S. Thongpang, K. W. Eliceiri, J. C. Williams, The effect of micro-ECoG substrate footprint on the meningeal tissue response. *J. Neural Eng.* **11**, 046011 (2014).
- J. Shin, Z. Liu, W. Bai, Y. Liu, Y. Yan, Y. Xue, I. Kandela, M. Pezrouh, M. R. MacEwan, Y. Huang, W. Z. Ray, W. Zhou, J. A. Rogers, Bioresorbable optical sensor systems for monitoring of intracranial pressure and temperature. *Sci. Adv.* **5**, eaaw1899 (2019).
- J. T. Caulfield, J. A. Wilson, N. K. Dhar, Spatial oversampling in imaging sensors: Benefits in sensitivity and detection, paper presented at the 2012 IEEE Applied Imagery Pattern Recognition Workshop (AIPR), Washington, DC, 9 to 11 October 2012.
- S. Kellis, L. Sorensen, F. Darvas, C. Sayres, K. O'Neill III, R. B. Brown, P. House, J. Ojemann, B. Greger, Multi-scale analysis of neural activity in humans: Implications for micro-scale electrocorticography. *Clin. Neurophysiol.* **127**, 591–601 (2016).
- L. Muller, L. S. Hamilton, E. Edwards, K. E. Bouchard, E. F. Chang, Spatial resolution dependence on spectral frequency in human speech cortex electrocorticography. *J. Neural Eng.* **13**, 056013 (2016).
- M. Gavish, D. L. Donoho, The optimal hard threshold for singular values is  $4/\sqrt{3}$ . *IEEE Trans. Inf. Theory* **60**, 5040–5053 (2014).
- I. W. Selesnick, Wavelet transform with tunable Q-factor. *IEEE Trans. Signal Processing* **59**, 3560–3575 (2011).
- M. Trumpis, M. Insanally, J. Zou, A. Elsharif, A. Ghomashchi, N. Sertac Artan, R. C. Froemke, J. Viventi, A low-cost, scalable, current-sensing digital headstage for high channel count  $\mu$ ECoG. *J. Neural Eng.* **14**, 026009 (2017).

34. P. P. Mitra, B. Pesaran, Analysis of dynamic brain imaging data. *Biophys. J.* **76**, 691–708 (1999).
35. A. P. Georgopoulos, A. B. Schwartz, R. E. Kettner, Neuronal population coding of movement direction. *Science* **233**, 1416–1419 (1986).
36. A. Arieli, A. Grinvald, H. Slovin, Dural substitute for long-term imaging of cortical activity in behaving monkeys and its clinical implications. *J. Neurosci. Methods* **114**, 119–133 (2002).
37. M. C. Wiest, M. A. L. Nicolelis, Behavioral detection of tactile stimuli during 7–12 Hz cortical oscillations in awake rats. *Nat. Neurosci.* **6**, 913–914 (2003).
38. A. Fontanini, D. B. Katz, 7 to 12 Hz activity in rat gustatory cortex reflects disengagement from a fluid self-administration task. *J. Neurophysiol.* **93**, 2832–2840 (2005).
39. M. A. Nicolelis, L. A. Baccala, R. C. Lin, J. K. Chapin, Sensorimotor encoding by synchronous neural ensemble activity at multiple levels of the somatosensory system. *Science* **268**, 1353–1358 (1995).
40. B. A. Hollenberg, C. D. Richards, R. Richards, D. F. Bahr, D. M. Rector, A MEMS fabricated flexible electrode array for recording surface field potentials. *J. Neurosci. Methods* **153**, 147–153 (2006).
41. A. M. Benison, D. M. Rector, D. S. Barth, Hemispheric mapping of secondary somatosensory cortex in the rat. *J. Neurophysiol.* **97**, 200–207 (2007).
42. K. Molina-Luna, M. M. Buitrago, B. Hertler, M. Schubring, F. Haiss, W. Nisch, J. B. Schulz, A. R. Luft, Cortical stimulation mapping using epidurally implanted thin-film microelectrode arrays. *J. Neurosci. Methods* **161**, 118–125 (2007).
43. J. Kim, J. Adam Wilson, J. C. Williams, A cortical recording platform utilizing  $\mu$ ECoG electrode arrays, in *2007 29th Annual International Conference of the IEEE Engineering in Medicine and Biology Society (IEEE, 2007)*, pp. 5353–5357.
44. B. Rubehn, C. Bosman, R. Oostenveld, P. Fries, T. Stieglitz, A MEMS-based flexible multichannel ECoG-electrode array. *J. Neural Eng.* **6**, 036003 (2009).
45. P. Ledochowitsch, R. J. Félus, R. R. Gibboni, A. Miyakawa, S. Bao, M. M. Maharbiz, Fabrication and testing of a large area, high density, parylene MEMS  $\mu$ ECoG array, paper presented at the *2011 IEEE 24th International Conference on Micro Electro Mechanical Systems*, Cancun, Mexico, 23 to 27 Jan. 2011.
46. G. Hotson, D. P. McMullen, M. S. Fifer, M. S. Johannes, K. D. Katyal, M. P. Para, R. Armiger, W. S. Anderson, N. V. Thakor, B. A. Wester, N. E. Crone, Individual finger control of a modular prosthetic limb using high-density electrocorticography in a human subject. *J. Neural Eng.* **13**, 026017 (2016).
47. D. Khodagholy, J. N. Gelinis, Z. Zhao, M. Yeh, M. Long, J. D. Greenlee, W. Doyle, O. Devinsky, G. Buzsáki, Organic electronics for high-resolution electrocorticography of the human brain. *Sci. Adv.* **2**, e1601027 (2016).
48. G. K. Anumanchipalli, J. Chartier, E. F. Chang, Speech synthesis from neural decoding of spoken sentences. *Nature* **568**, 493–498 (2019).

**Acknowledgments:** Y.H. acknowledges support from the NSF (CMMI-1635443). Y.X. gratefully acknowledges support from the Ryan Fellowship and the Northwestern University International Institute for Nanotechnology. K.S. and H.F. acknowledge support from a Samsung Global Research Outreach Award. F.V. acknowledges support from the Citizens United for Research in Epilepsy Taking Flight Award. K.J.Y. acknowledges support from the support from the National Research Foundation of Korea (grant nos. NRF-2018M3A7B4071109 and NRF-2019R1A2C2086085). B.H.K. acknowledges support from Creative Materials Discovery Program and Nano-Material Technology Development Program through the National Research Foundation of Korea (NRF) funded by Ministry of Science and ICT (NRF-2018M3D1A1058972, no. 2019R1G1A1100737, 2009-0082580). **Funding:** This work was funded by a National Institute of Neurological Disorders and Stroke award U01 NS099697 to J.V., B.P., J.A.R., and K.S.; a National Science Foundation award CCF1422914 to J.V.; a National Science Foundation award CCF-1564051 to J.V.; a Steven W. Smith Fellowship to B.B.; a L'Oreal USA for Women in Science Fellowship to A.L.O.; and Defense Advanced Research Programs Agency awards DARPA-BAA-16-09 to K.S., B.P., J.A.R., and J.V., and DARPA-BAA-13-20 to B.P., J.A.R., and J.V. **Author contributions:** C.-H.C., S.M.W., A.L.O., and K.J.Y. contributed equally to the work. C.-H.C., S.M.W., A.L.O., K.J.Y., B.P., J.A.R., and J.V. designed the experiments. C.-H.C., S.M.W., K.J.Y., C.W., S.M., J.L., K.J.S., B.H.K., S.B.K., and H.F. designed, tested, and provided devices. Y.X. and Y.H. contributed mechanical simulations. M.T., C.-H.C., B.B., V.W., C.Y., F.V., and A.R. performed experiments in rodents and analyzed the data. A.L.O. and B.P. performed experiments in NHPs and analyzed the data. R.H. and K.S. contributed FIB measurements. C.-H.C., S.M.W., A.L.O., K.J.Y., M.T., B.P., J.A.R., and J.V. wrote the manuscript. J.V., J.A.R., B.P., and K.S. secured funds for this project. **Competing interests:** Parts of the technology described here are patented under “Conformable Actively Multiplexed High-Density Surface Electrode Array for Brain Interfacing,” U.S. Patent No. 8,934,965; “Flexible and Scalable Sensor Arrays for Recording and Modulating Physiologic Activity,” U.S. Patent Nos. 9,107,592 and 9,839,367, and European Patent No. 2265171; and “Conformable Actively Multiplexed High-Density Surface Electrode Array for Brain Interfacing,” U.S. Patent No. 10,349,860. The authors declare that they have no other competing interests. **Data and materials availability:** The data and code that support the findings of this study are archived on Zenodo (DOI: 10.5281/zenodo.3686317). All other data are present in the paper or the Supplementary Materials.

Submitted 21 June 2019  
 Accepted 28 February 2020  
 Published 8 April 2020  
 10.1126/scitranslmed.aay4682

**Citation:** C.-H. Chiang, S. M. Won, A. L. Orsborn, K. J. Yu, M. Trumpis, B. Bent, C. Wang, Y. Xue, S. Min, V. Woods, C. Yu, B. H. Kim, S. B. Kim, R. Huq, J. Li, K. J. Seo, F. Vitale, A. Richardson, H. Fang, Y. Huang, K. Shepard, B. Pesaran, J. A. Rogers, J. Viventi, Development of a neural interface for high-definition, long-term recording in rodents and nonhuman primates. *Sci. Transl. Med.* **12**, eaay4682 (2020).

## Development of a neural interface for high-definition, long-term recording in rodents and nonhuman primates

Chia-Han Chiang, Sang Min Won, Amy L. Orsborn, Ki Jun Yu, Michael Trumpis, Brinnae Bent, Charles Wang, Yeguang Xue, Seunghwan Min, Virginia Woods, Chunxiu Yu, Bong Hoon Kim, Sung Bong Kim, Rizwan Huq, Jinghua Li, Kyung Jin Seo, Flavia Vitale, Andrew Richardson, Hui Fang, Yonggang Huang, Kenneth Shepard, Bijan Pesaran, John A. Rogers and Jonathan Viventi

*Sci Transl Med* 12, eaay4682.  
DOI: 10.1126/scitranslmed.aay4682

### Recording in high resolution

Recording large number of neural signals in real time with high definition for long periods of time is necessary for understanding brain physiology and disease pathophysiology. Unfortunately, current brain interface devices only allow recordings of small brain areas with limited number of electrodes. Here, Chiang *et al.* developed a neural interface device, called Neural Matrix, that allowed stable in vivo neural recordings with high throughput in rodents and nonhuman primates. The system provided stable recordings projected to last for 6 years after implantation. The Neural Matrix will be useful for the study of brain physiology in preclinical setting and might be scalable to humans for clinical purposes.

#### ARTICLE TOOLS

<http://stm.sciencemag.org/content/12/538/eaay4682>

#### SUPPLEMENTARY MATERIALS

<http://stm.sciencemag.org/content/suppl/2020/04/06/12.538.eaay4682.DC1>

#### RELATED CONTENT

<http://stm.sciencemag.org/content/scitransmed/11/521/eaaw8954.full>  
<http://stm.sciencemag.org/content/scitransmed/9/411/eaah6756.full>  
<http://stm.sciencemag.org/content/scitransmed/7/282/282ra46.full>

#### REFERENCES

This article cites 43 articles, 5 of which you can access for free  
<http://stm.sciencemag.org/content/12/538/eaay4682#BIBL>

#### PERMISSIONS

<http://www.sciencemag.org/help/reprints-and-permissions>

Use of this article is subject to the [Terms of Service](#)

---

*Science Translational Medicine* (ISSN 1946-6242) is published by the American Association for the Advancement of Science, 1200 New York Avenue NW, Washington, DC 20005. The title *Science Translational Medicine* is a registered trademark of AAAS.

Copyright © 2020 The Authors, some rights reserved; exclusive licensee American Association for the Advancement of Science. No claim to original U.S. Government Works